

GEOMETRICALLY DERIVED TIMESCALES FOR STAR FORMATION IN SPIRAL GALAXIES

D. TAMBURRO, H.-W. RIX AND F. WALTER

Max-Planck-Institut für Astronomie, Königstuhl 17, D-69117 Heidelberg, Germany

E. BRINKS

Centre for Astrophysics Research, University of Hertfordshire, College Lane, Hatfield AL10 9AB, United Kingdom

W.J.G. DE BLOK

Department of Astronomy, University of Cape Town, Private Bag X3, Rondebosch 7701, South Africa

R.C. KENNICUTT

Institute of Astronomy, University of Cambridge, Madingley Road, Cambridge CB3 0HA, United Kingdom

AND

M.-M. MAC LOW¹

Department of Astrophysics, American Museum of Natural History, 79th Street and Central Park West, New York, NY 10024-5192, USA

Accepted for publication in the AJ special THINGS issue. For a high-resolution version visit: <http://www.mpia.de/THINGS/Publications.html>

ABSTRACT

We estimate a characteristic timescale for star formation in the spiral arms of disk galaxies, going from atomic hydrogen (HI) to dust-enshrouded massive stars. Drawing on high-resolution HI data from The HI Nearby Galaxy Survey and 24 μm images from the *Spitzer* Infrared Nearby Galaxies Survey we measure the average angular offset between the HI and 24 μm emissivity peaks as a function of radius, for a sample of 14 nearby disk galaxies. We model these offsets assuming an instantaneous kinematic pattern speed, Ω_p , and a timescale, $t_{\text{HI} \rightarrow 24 \mu\text{m}}$, for the characteristic time span between the dense HI phase and the formation of massive stars that heat the surrounding dust. Fitting for Ω_p and $t_{\text{HI} \rightarrow 24 \mu\text{m}}$, we find that the radial dependence of the observed angular offset (of the HI and 24 μm emission) is consistent with this simple prescription; the resulting corotation radii of the spiral patterns are typically $R_{\text{cor}} \simeq 2.7R_s$, consistent with independent estimates. The resulting values of $t_{\text{HI} \rightarrow 24 \mu\text{m}}$ for the sample are in the range 1–4 Myr. We have explored the possible impact of non-circular gas motions on the estimate of $t_{\text{HI} \rightarrow 24 \mu\text{m}}$ and have found it to be substantially less than a factor of 2. This implies that a short timescale for the most intense phase of the ensuing star formation in spiral arms, and implies a considerable fraction of molecular clouds exist only for a few Myr before forming stars. However, our analysis does not preclude that some molecular clouds persist considerably longer. If much of the star formation in spiral arms occurs within this short interval $t_{\text{HI} \rightarrow 24 \mu\text{m}}$, then star formation must be inefficient, in order to avoid the short-term depletion of the gas reservoir.

Subject headings: galaxies: evolution – galaxies: ISM – galaxies: kinematics and dynamics – galaxies: spiral – stars: formation

1. INTRODUCTION

Roberts (1969, hereafter R69) was the first to develop the scenario of spiral-arm-driven star formation in galaxy disks. In this picture a spiral density wave induces gravitational compression and shocks in the neutral hydrogen gas, which in turn leads to the collapse of (molecular) gas clouds that results in star formation. This work already pointed out the basic consequences for the relative

geometry of the dense cold gas reservoir² and the emergent young stars: when viewed from a reference frame that corotates with the density wave, the densest part of the atomic hydrogen (HI) lies at the shock (or just upstream from it), while the young stars lie downstream from the density wave. Using HI and H α as the tracers of the cold gas and of the young stars, respectively, R69 found a qualitative support in the data available at the time. In this picture, the characteristic timescale for this sequence of events is reflected in the typical angular offset, at a given radius, between tracers of the different stages of spiral-arm-driven star formation.

While this qualitative picture has had continued popularity, quantitative tests of the importance of spiral den-

Electronic address: tamburro@mpia.de, rix@mpia.de, walter@mpia.de
Electronic address: e.brinks@herts.ac.uk
Electronic address: edeblok@circinus.ast.uct.ac.za
Electronic address: robk@ast.cam.ac.uk
Electronic address: mordecai@amnh.org

¹ also Max-Planck-Institut für Astronomie, and Institut für Theoretische Astrophysik, Zentrum für Astronomie der Universität Heidelberg

² This paper pre-dates observational studies of molecular gas in galaxies.

sity waves as star-formation trigger (Lin & Shu 1964) and of the timescales for the ensuing star formation have proven complicated. First, it has become increasingly clear that even in galaxies with grand-design spiral arms, about half of the star formation occurs in locations outside the spiral arms (Elmegreen & Elmegreen 1986). Second, stars formed from molecular clouds (not directly from HI) and very young star clusters are dust enshrouded at first. Moreover, the actual physical mechanism that appears to control the rate and overall location of star formation in galaxies is the gravitational instability of the gas and existing stars (e.g. Li, Mac Low, & Klessen 2005). Stars only form above a critical density (Martin & Kennicutt 2001) which is consistent with the predicted Toomre (1964) criterion for gravitational instability as generalized by Rafikov (2001). Although, in galaxies with prominent spiral structure local gas condensations are governed by magneto-rotational instabilities—spiral arms are regions of low shear where the transfer of angular momentum is carried out by magnetic fields (Kim & Ostriker 2002, 2006). Obtaining high-resolution, sensitive maps of all phases in this scenario (HI, molecular gas, dust-enshrouded young stars, unobscured young stars) has proven technically challenging.

If the star formation originates from direct collapse of gravitationally unstable gas, and if the rotation curve and approximate pattern speed of the spiral arms are known, the geometric test suggested by R69 provides a timescale for the end-to-end (from HI to young stars) process of star formation. Of course, there are other ways of estimating the timescales that characterize the evolutionary sequence of the interstellar medium (ISM), based on other physical arguments. However, other lines of reasoning have led to quite a wide range of varying lifetime estimates as discussed below.

Offsets between components such as CO and H α emission in the disks of spiral galaxies have indeed been observed (Vogel, Kulkarni, & Scoville 1988; Garcia-Burillo, Guelin, & Cernicharo 1993; Rand & Kulkarni 1990; Scoville et al. 2001). Mouschovias, Tassis, & Kunz (2006) remarked that the angular separation between the dust lanes and the peaks of H α emission found for nearby spiral galaxies (e.g. observed by Roberts 1969; Rots 1975) implied timescales of the order of 10 Myr. More recently Egusa, Sofue, & Nakanishi (2004), using the angular offset between CO and H α in nearby galaxies, derived $t_{\text{CO} \rightarrow \text{H}\alpha} \simeq 4.8$ Myr.

Observationally, the HI surface density is found to correlate well with sites of star formation and emission from molecular clouds (Wong & Blitz 2002; Kennicutt 1998). The conversion timescale of HI \rightarrow H $_2$ is a key issue since it determines how well the peaks of HI emission can be considered as potential early stages of star formation. H $_2$ molecules only form on dust grain surfaces in dusty regions that shield the molecules from ionizing UV photons. Their formation facilitates the subsequent building up of more complex molecules (e.g. Williams 2005). Within shielded clouds the conversion timescale HI \rightarrow H $_2$ is given by $\tau_{\text{H}_2} \sim 10^9/n_0$ yr, where n_0 is the proton density in cm^{-3} (Hollenbach & Salpeter 1971; Jura 1975; Goldsmith & Li 2005; Goldsmith, Li, & Krco 2007). Given the inverse proportionality with n_0 , the

conversion timescale can vary from the edge of a molecular cloud ($\tau \simeq 4 \times 10^6$ yr, $n_0 \sim 10^3$) to the central region ($\tau \sim 10^5$ yr, $n_0 \sim 10^4$) where the density is higher. Local turbulent compression can further enhance the local density, and thus decrease the conversion timescale (Glover & Mac Low 2007). Thus, even short cloud-formation timescales remain consistent with the HI \rightarrow H $_2$ conversion timescale.

The subsequent evolution (see e.g. Beuther et al. 2007, for a review) involves the formation of cloud cores (initially starless) and then star cluster formation through accretion onto protostars, which finally become main sequence stars. High-mass stars evolve more rapidly than low-mass stars. Stars with $M \geq 5M_\odot$ reach the main sequence quickly, in less than 1 Myr (Hillenbrand et al. 1993; Palla & Stahler 1999), while they are still deeply embedded and actively accreting. The O and B stars begin to produce an intense UV flux that photoionizes the surrounding dusty environment within a few Myr, and subsequently become optically visible (Thronson & Telesco 1986).

A different scenario is suggested by Allen (2002), in which young stars in the disks of galaxies produce HI from their parent H $_2$ clouds by photodissociation. According to this scenario, the HI should not be seen furthest upstream in the spiral arm, but rather between the CO and UV/H α regions. Allen et al. (1986) indeed report observation of HI downstream of dust lanes in M83.

Several lines of reasoning, however, point toward longer star-formation timescales and molecular cloud lifetimes, much greater than 10 Myr. Krumholz & McKee (2005) conclude that the star-formation rate in the solar neighborhood is low. In fact, they point out that the star-formation rate in the solar neighborhood is ~ 100 times smaller than the ratio of the masses of nearby molecular clouds to their free-fall time $M_{\text{MC}}/\tau_{\text{ff}}$, which also indicates the rate of compression of molecular clouds. Individual dense molecular clouds have been argued to stay in a fully molecular state for about 10-15 Myr before their collapse (Tassis & Mouschovias 2004), and to transform about 30% of their mass into stars in $\geq 7 \tau_{\text{ff}}$ ($\sim 10^6$ yr e.g. considering the mass of the Orion Nebula Cluster, ONC Tan, Krumholz, & McKee 2006). Large molecular clouds have been calculated to survive 20 to 30 Myr before being destroyed by the stellar feedback by Krumholz, Matzner, & McKee (2006). Based on observations, Palla & Stahler (1999, 2000) argue that the star formation rate in the ONC was low 10^7 yr ago, and that it increased only recently. Blitz et al. (2007), using a statistical comparison of cluster ages in the Large Magellanic Cloud (LMC) to the presence of CO, found that the lifetime for giant molecular clouds is 20–30 Myr.

However, other studies conclude that the timescales for star-formation are rather short. Hartmann (2003) pointed out that the Palla–Stahler model is not consistent with observations since most of the molecular clouds in the ONC are forming stars at the same high rate. The stellar age or the age spread in young open stellar clusters is not necessarily a useful constraint on the star-formation timescale: the age spread, for example, may result from independent and non-simultaneous bursts of star-formation (Elmegreen 2000). Ballesteros-Paredes & Hartmann (2007) pointed out that the molecular cloud life-

time must be shorter than the value of $\tau_{\text{MC}} \simeq 10$ Myr suggested by Mouschovias, Tassis, & Kunz (2006). Also subsequent star formation must proceed very quickly, within a few Myr (Vázquez-Semadeni et al. 2005; Hartmann, Ballesteros-Paredes, & Bergin 2001). Prescott et al. (2007) found strong association between 24 μm sources and optical H II regions in nearby spiral galaxies. This provides constraints on the lifetimes of star-forming clouds: the break out time of the clouds and their parent clouds is less or at most of the same order as the lifetime of the H II regions, therefore a few Myr. Dust and gas clouds must dissipate on a timescale no longer than 5–10 Myr.

In conclusion, all the previous studies listed aim to estimate the lifetimes of molecular clouds or the timescale separation between the compression of neutral gas and newly formed stars. Most of these studies are based on observations of star-forming regions both in the Milky Way and in external galaxies, and in all cases the derived timescales lie in a range between a few Myr and several tens of Myr.

In this paper, we examine a new method (§ 2) for estimating the timescale to proceed from HI compression to star formation in nearby spiral galaxies. We compare *Spitzer Space Telescope*/MIPS 24 μm data from the *Spitzer* Near Infrared Galaxies Survey (SINGS; Kennicutt et al. 2003) to 21 cm maps from the HI Nearby Galaxy Survey (THINGS; Walter et al. 2008). The proximity of our targets allows for high spatial resolution. In § 3 we give a description of the data. The MIPS bands (24, 70 and 160 μm) are tracers of warm dust heated by UV and are therefore good indicators of recent star-formation activity (see for example Dale et al. 2005). We used the band with the best resolution, 24 μm , which has been recognized as the best of the *Spitzer* bands for tracing star formation (Calzetti et al. 2005, 2007; Prescott et al. 2007); the 8 μm *Spitzer*/IRAC band has even higher resolution but is contaminated by PAH features that undergo strong depletion in the presence of intense UV radiation (Dwek 2005; Smith et al. 2007). In § 4 we describe how we use azimuthal cross-correlation to compare the HI and 24 μm images and derive the angular offset of the spiral pattern. This algorithmic approach minimizes possible biases introduced by subjective assessments. We describe our results in § 5 where we derive $t_{\text{HI} \rightarrow 24 \mu\text{m}}$ for our selection of objects. Finally, we discuss the implications of our results in § 6 and draw conclusions in § 7.

2. METHODOLOGY

The main goal of this paper is to estimate geometrically the timescales for spiral-arm-driven star formation using a simple kinematic model, examining the R69 arguments in light of state-of-the-art data. Specifically, we set out to determine the relative geometry of two tracers for different stages of star-formation sequence in a sample of nearby galaxies, drawing on the SINGS and THINGS data sets (see § 3): the 24 μm and the HI emission.

While the angular offset between these two tracers is an empirical model-independent measurement, a conversion into a star-formation timescale assumes (a) that peaks of the HI trace material that is forming molecular clouds, and (b) that the peaks of the 24 μm emission trace the very young, still dust-enshrouded star clus-

ters, where their UV emission is absorbed and re-radiated into the mid- to far-infrared wavelength range ($\sim 5 \mu\text{m}$ to $\sim 500 \mu\text{m}$). The choice of these particular tracers was motivated by the fact that they should tightly bracket the conversion process of molecular gas into young massive stars, and by the availability of high-quality data from the SINGS and THINGS surveys. Note that a number of imaging studies in the near-IR have shown (e.g. Rix & Zaritsky 1995) that the large majority of luminous disk galaxies have a coherent, dynamically relevant spiral arm density perturbation. Therefore, this overall line of reasoning can sensibly be applied to a sample of disk galaxies.

We consider a radius in the galaxy disk where the spiral pattern can be described by a kinematic pattern speed, Ω_p , and the local circular velocity $v_c(r) \equiv \Omega(r) \times r$. Then two events separated by a time $t_{\text{HI} \rightarrow 24 \mu\text{m}}$ will have a phase offset of

$$\Delta\phi(r) = (\Omega(r) - \Omega_p) t_{\text{HI} \rightarrow 24 \mu\text{m}}, \quad (1)$$

where $t_{\text{HI} \rightarrow 24 \mu\text{m}}$ denotes the time difference between two particular phases that we will study here. If the spiral pattern of a galaxy indeed has a characteristic kinematic pattern speed, the angular offset between any set of tracers is expected to vary as a function of radius in a characteristic way. Considering the chronological sequence, defining the angular phase difference $\Delta\phi \equiv \phi_{24 \mu\text{m}} - \phi_{\text{HI}}$ and adopting the convention that ϕ increases in the direction of rotation, we expect the qualitative radial dependence plotted in Figure 1: $\Delta\phi > 0$ where the galaxy rotates faster than the pattern speed, otherwise $\Delta\phi < 0$. Where $\Omega(R_{\text{cor}}) = \Omega_p$, at the so-called corotation radius, we expect the sign of $\Delta\phi$ to change.

In practice, the gaseous and stellar distribution is much more complex than in the qualitative example of Figure 1, since the whole spiral network, even for galaxies where the spiral arms are well defined such as in grand-design galaxies, typically exhibits a full wealth of smaller scale sub-structures both in the arms and in the inter-arm regions. The optimal method to measure the angular offset between the two observed patterns is therefore through cross-correlation (§ 4). We treat the timescale $t_{\text{HI} \rightarrow 24 \mu\text{m}}$ and the present-day pattern speed Ω_p as global constants for each galaxy, although these two parameters might, in principle, vary as function of galactocentric radius. Note that we need not to rely on the assumption that the spiral structure is quasi-stationary over extended periods, $t \geq t_{\text{dyn}}$. Even if spiral arms are quite dynamic, continuously forming and breaking, and with a pattern speed varying with radius, our analysis will hold approximately.

3. DATA

The present analysis is based on the 21 cm emission line maps, a tracer of the neutral atomic gas for the 14 disk galaxies listed in Table 1, which are taken from THINGS. These high-quality NRAO³ Very Large Array observations provide data cubes with an angular resolution of $\simeq 6''$ and spectral resolution of 2.6 or 5.2 km s^{-1} . Since the target galaxies are nearby, at distances of 3–10 Mpc, the linear resolution of the maps corresponds

³ The National Radio Astronomy Observatory is a facility of the National Science Foundation operated under cooperative agreement by Associated Universities, Inc.

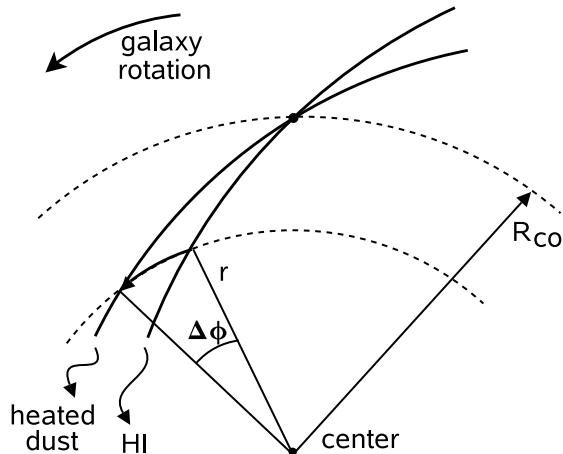


FIG. 1.— Schematic geometry adopted to derive the azimuthal phase difference $(\phi_{24\mu\text{m}} - \phi_{\text{HI}})(r) \equiv \Delta\phi(r)$ between the HI and the $24\mu\text{m}$ emission, with ϕ increasing in the direction of rotation. The sketch shows part of a face-on galaxy rotating anti-clockwise, with the center as indicated. The solid curved lines represent the two components within one spiral arm, namely the HI and the heated dust. The angular separation between the two components is exaggerated for clarity. We measured the deprojected phase difference $\Delta\phi(r)$ at a given radius. Inside corotation, R_{cor} , the material is rotating faster than the pattern speed and the $24\mu\text{m}$ emission lies ahead of the HI ($\phi_{\text{HI}} < \phi_{24\mu\text{m}}$). At corotation the two patterns coincide, and outside R_{cor} the picture is reversed since the pattern speed exceeds the rotation of the galaxy.

to 100–300 pc. The HI data cubes of our target galaxies are complemented with near-IR images, which are public data. In particular, the majority of the THINGS galaxies (including all those in Table 1) have also been observed within the framework of the SINGS and we make an extensive use of the $24\mu\text{m}$ MIPS images (see § 4.2). Figure 2 illustrates our data for two of the sample galaxies, NGC 5194 and NGC 2841. The $24\mu\text{m}$ band image is shown in color scale, and the contours show the HI emission map. To obtain the exponential scale length of the stellar disk (see § 4), we use $3.6\mu\text{m}$ Infrared Array Camera (IRAC) images when available, otherwise we use H band images taken from the Two Micron All Sky Survey (2MASS; Jarrett et al. 2003). To check the consistency of our results, we use CO maps from the Berkeley-Illinois-Maryland Association Survey Of Nearby Galaxies (BIMA-SONG Helfer et al. 2003) for some of our target galaxies.

4. ANALYSIS

All analysis in this paper started from fully reduced images and data cubes. On this data we carry out two main steps. First, we derive the rotation curve $v_c(r)$ of the HI and the geometrical projection parameters of the galaxy disk, and use these parameters to deproject the maps of the galaxies to face-on orientation (see Table 1). Second, we sample the face-on maps in concentric annuli. For each annulus we cross-correlate the corresponding pair of HI and $24\mu\text{m}$ fluxes, in order to derive the angular offset between the HI and the $24\mu\text{m}$ patterns as a function of radius.

For three of the galaxies listed in Table 1 (NGC 628, NGC 5194, and NGC 3627), we also measure the angular offset between the CO and $24\mu\text{m}$ emission maps. If the ISM evolves sequentially from atomic into molecular gas, and then subsequently initiates the formation of stars, considering the kinematics expressed in Eq. 1, we expect

the CO emission to lie in between the HI and the $24\mu\text{m}$.

4.1. Analysis of the HI Kinematics

For each object we apply the same general approach: we first perform adaptive binning of the HI data cube regions with low signal-to-noise (S/N) ratio using the method described by Cappellari & Copin (2003). From the resulting spatially binned data cubes we fit the 21 cm emission lines with a single Gaussian profile and use the parameterization to derive (1) the line-of-sight velocity map $v(x, y)$, given by the line centroid, and (2) the flux maps $\mu_0(x, y) \equiv a(x, y)/(\sqrt{2\pi}\sigma(x, y))$, where a and σ are the Gaussian peak amplitude and width, respectively. Since we do not need to derive the rotation curve with high accuracy for the purpose of this paper, we limit our model to a co-planar rotating disk with circular orbits described by

$$v(x, y) = v_{\text{sys}} + v_c(r) \sin i \cos \psi, \quad (2)$$

where $v(x, y)$ is the observed velocity map along the line of sight (see Begeman 1989). For simplicity, we assume here that the orbits are circular, though we address the issue of non-circular motions in § 5.4. By χ^2 minimization fitting⁴ of the model function in Eq. 2 to the observed velocity map $v(x, y)$, we obtain the systemic velocity $v_{\text{sys}} = \text{const}$, the inclination i and the position angle (P.A.) of the geometric projection of the disk on to the sky. Here, ψ is the azimuthal angle on the plane of the inclined disk (not the sky) and is a function of i and P.A. The line where $\psi = 0$ denotes the orientation of the line of nodes on the receding side of the disk. The kinematic center (x_0, y_0) is fixed a priori and is defined as the central peak of either the IRAC $3.6\mu\text{m}$ or the 2MASS H band image. The positions of the dynamical centers used here are consistent with those derived in Trachternach et al. (2008). We parameterize the deprojected rotation curve v_c with a four-parameter arctan-like function (e.g., Rix et al. 1997)

$$v_c(r) = v_0 (1 + x)^\beta (1 + x^{-\gamma})^{-1/\gamma}, \quad (3)$$

where $x = r/r_0$. Here, r_0 is the turn-over radius, v_0 is the scale velocity, γ determines the sharpness of the turnover and β is the asymptotic slope at larger radii.

The values for the projection parameters i , and P.A., the systemic velocity v_{sys} , and the asymptotic velocity that have been obtained applying the approach described above, are consistent with the values reported in Table 1. From the maximum value of Eq. 3 we obtain the maximum rotational velocity v_{max} , which is listed for all the sample galaxies in Table 1.

4.2. Azimuthal Cross-Correlation

The central analysis step is to calculate by what angle $\Delta\phi$ the patterns of HI and $24\mu\text{m}$ need to be rotated with respect to each other in order to best match. We use the kinematically determined orientation parameters, i and P.A., to deproject both the HI and $24\mu\text{m}$ images to face-on. To estimate the angular offset $\Delta\phi$ between the two flux images at each radius, we divide the face-on

⁴ The fitting has been performed with the `mpfit` IDL routine found at the URL: <http://cow.physics.wisc.edu/~craigm/idl/fitting.html>

TABLE 1
 THINGS AND SINGS TARGET GALAXIES

Obj. Name	Alt. Name	R_{25} (') (1)	R_s (') (2)	Band (3)	i (°) (4)	P.A. (°) (5)	D (Mpc) (6)	v_{\max} (km s ⁻¹) (7)
NGC 2403		9.98	1.30*	H	63	124	3.22	128
NGC 2841		3.88	0.92*	3.6	74	153	14.1	331
NGC 3031	M81	10.94	3.63 ± 0.2	3.6	59	330	3.63	256
NGC 3184		3.62	0.92 ± 0.09	H	16	179	11.1	260
NGC 3351		3.54	0.86 ± 0.03	3.6	41	192	9.33	210
NGC 3521		4.8	0.74 ± 0.02	3.6	73	340	10.05	242
NGC 3621		5.24	0.80*	H	65	345	6.64	144
NGC 3627	M66	4.46	0.95*	3.6	62	173	9.25	204
NGC 5055	M63	6.01	1.16 ± 0.05	H	59	102	7.82	209
NGC 5194	M51	3.88	1.39 ± 0.11	H	42	172	7.77	242
NGC 628	M74	4.77	1.10 ± 0.09	H	7	20	7.3	220
NGC 6946		5.35	1.73 ± 0.07	H	32.6	242	5.5	201
NGC 7793		5.0	1.16 ± 0.05	H	50	290	3.82	109
NGC 925		5.23	1.43*	3.6	66	286	9.16	121

NOTE. — Semi-major axis of the 25 mag arcsec⁻² isophote in the B band obtained from the LEDA database (URL: <http://leda.univ-lyon1.fr/>); (2) exponential scale length derived in this paper as described in § 4 using either IRAF or `galfit` (values tagged with *), where the error bars are $\delta R_s/R_s < 1\%$; (3) image band used (2MASS H or IRAC 3.6 μm band) to derive R_s ; (4) and (5) kinematic inclination and P.A., respectively; (6) adopted distance; (7) maximum amplitude of the rotation velocity corrected for inclination obtained from the rotation curve v_c derived in § 4.1. The values in Columns (4) to (6) are adopted from de Blok et al. (2008).

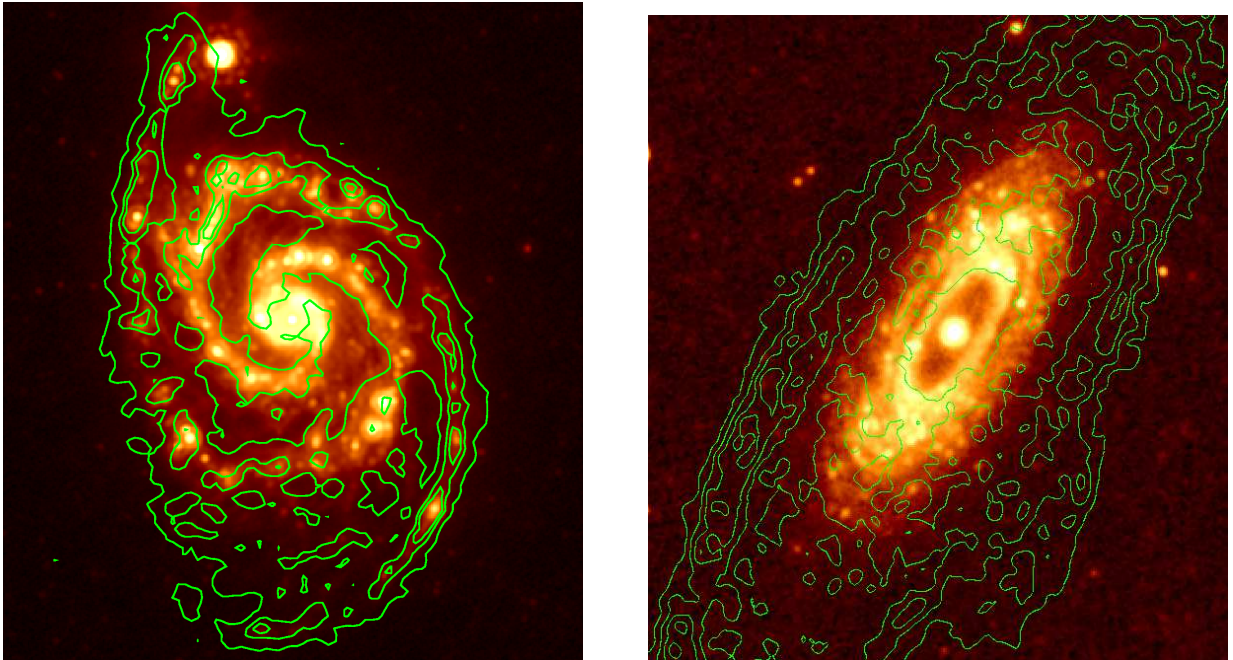


FIG. 2.— The 24 μm band image is plotted in color scale for the galaxies NGC 5194 (left) and NGC 2841 (right); the respective HI emission map is overlaid with green contours.

images into concentric rings of width $\sim 5''$ and extract the flux within this annulus as a function of azimuth. We then use a straightforward cross-correlation (CC) to search for phase lags in $f_{\text{HI}}(\phi|r)$ versus $f_{24\mu\text{m}}(\phi|r)$. In general, the best match between two discrete vectors x and y is realized by minimizing as a function of the phase shift ℓ (also defined as *lag*) the quantity

$$\chi_{x,y}^2(\ell) = \sum_k [x_k - y_{k-\ell}]^2, \quad (4)$$

where the sum is calculated over all the N elements of x and y with $k = 0, 1, 2, \dots, N - 1$. Specifically here, for a given radius $r = \hat{r}$ we consider for all discrete values of azimuth ϕ :

$$x_k = f_{\text{HI}}(\phi_k|\hat{r}) \quad \text{and} \quad y_{k-\ell} = f_{24\mu\text{m}}(\phi_{k-\ell}|\hat{r}). \quad (5)$$

Expanding the argument of the sum in Eq. 4 one obtains that $\chi^2(\ell)$ is independent of the terms $\sum_k x_k^2$ and $\sum_k y_{k-\ell}^2$, and χ^2 is minimized by the maximization of

$$cc_{x,y}(\ell) = \sum_k [x_k y_{k-\ell}], \quad (6)$$

which is defined as the CC coefficient. Here we used the normalized CC

$$cc_{x,y}(\ell) = \frac{\sum_k [(x_k - \bar{x})(y_{k-\ell} - \bar{y})]}{\sqrt{\sum_k (x_k - \bar{x})^2 \sum_k (y_{k-\ell} - \bar{y})^2}}, \quad (7)$$

where \bar{x} and \bar{y} are the mean values of x and y respectively. Here the slow, direct definition has been used and not the fast Fourier transform method. The vectors are wrapped around to ensure the completeness of the comparison. With this definition the CC coefficient would

have a maximum value of unity for identical patterns, while for highly dissimilar patterns it would be much less than 1. We apply the definition in Eq. 7 using the substitutions of Eq. 5 to compute the azimuthal CC coefficient $cc(\ell)$ of the HI and the 24 μm images. The best match between the HI and the 24 μm signals is realized at a value ℓ_{max} such that $cc(\ell_{\text{max}})$ has its peak value. Since the expected offsets are small (only a few degrees) we search the local maximum around $\ell \simeq 0$. The method is illustrated in Figure 3, which shows that $cc(\ell)$ has several peaks, as expected due to the self-similarity of the spiral pattern.

We consider a range that encompasses the maximum of the $cc(\ell)$ profile, i.e. the central ~ 100 – 150 data points around ℓ_{max} . This number, depending on the angular size of the ring, is dictated by the azimuthal spread of the spiral arms and the number of substructures (e.g., dense gas clouds, star clusters, etc.) per unit area. This corresponds, for example, to a width in ℓ of a few tens of degrees at small radii ($\sim 1'$), depending on the distance of the object, and a range in width of ℓ decreasing linearly with the radius. We interpolate $cc(\ell)$ around ℓ_{max} with a fourth-degree polynomial using the following approximation: $cc(\ell) \simeq p_4(\ell) = \sum_{n=0}^4 a_n \ell^n$ and calculate numerically (using the Python⁵ package `scipy.optimize`) the peak value at ℓ_{max} , $p_4(\ell_{\text{max}})$. By repeating the procedure for all radii, the angular offset HI \rightarrow 24 μm results in $\Delta\phi(r) = -\ell_{\text{max}}(r)$. The direction or equivalently the sign of the lag ℓ_{max} between two generic vectors x and y depends on the order of x and y in the definition of the CC coefficient. Note that $cc_{x,y}(\ell)$ in Eq. 6 is not commutative for interchange of x and y , being $cc_{y,x}(\ell) = cc_{x,y}(-\ell)$. For $\ell_{\text{max}} = 0$ the two patterns best match at zero azimuthal phase shift. The error bars for $\delta\ell_{\text{max}}(r)$ have been evaluated through a Monte Carlo approach, adding normally distributed noise and assuming the expectation values of ℓ_{max} and $\delta\ell_{\text{max}}$ as the mean value and the standard deviation, respectively, after repeating the determination $N = 100$ times.

Our analysis is limited to the radial range between low S/N regions at the galaxy centers and their outer edges. In the HI emission maps the S/N is low near the galaxy center, where the HI is converted to molecular H_2 , whereas for the 24 μm band the emission map has low S/N near R_{25} (and in most cases already at $\sim 0.8 R_{25}$). Regions with S/N < 3 in either the HI or 24 μm images have been clipped. We also ignore those points ℓ_{max} with a coefficient $cc(\ell_{\text{max}})$ lower than a threshold $cc \simeq 0.2$. We further neglect any azimuthal ring containing less than a few hundred points, which occurs near the image center and near R_{25} . The resulting values $\Delta\phi(r)$ are shown in Figure 4.

4.3. Disk Exponential Scale Length

We also determine the disk exponential scale length R_s for our sample using the `galfit`⁶ algorithm (Peng et al. 2002). In particular, we fit an exponential disk profile and a de Vaucouleurs profile to either the IRAC 3.6 μm or to the 2MASS H band image. As `galfit` underestimates the error on R_s (as recognized by the author of the

algorithm), typically $\delta R_s/R_s < 1\%$, we therefore also use the IRAF task `ellipse` (Jedrzejewski 1987) to derive the radial surface brightness profile and fit R_s . After testing the procedure on a few objects, we note only small differences (of the order of the error bars in Table 1) when deriving R_s from the H band and the 3.6 μm band.

5. RESULTS

5.1. Angular Offset

With the angular offset $\Delta\phi(r) \equiv \langle \phi_{24\mu\text{m}} - \phi_{\text{HI}} \rangle(r)$, where ϕ increases in the direction of rotation, and the rotation curve $v_c(r)$ for each radial bin, we can rewrite Eq. 1 as

$$\Delta\phi(r) = \left(\frac{v_c(r)}{r} - \Omega_p \right) \times t_{\text{HI}\rightarrow 24\mu\text{m}}, \quad (8)$$

where $\Omega(r) \equiv v_c/r$. Since $\Omega(r) > \Omega_p$ inside the corotation radius R_{cor} , and $\Omega(r) < \Omega_p$ outside corotation, we expect $\Delta\phi(r) > 0$ for $r < R_{\text{cor}}$ and $\Delta\phi(r) < 0$ for $r > R_{\text{cor}}$. At corotation, where $\Delta\phi(R_{\text{cor}}) = 0$, the two components HI and 24 μm should have no systematic offset. We assume $t_{\text{HI}\rightarrow 24\mu\text{m}}$ and Ω_p to be constant for any given galaxy, and that all the spirals are trailing, since the only spiral galaxies known to have a leading pattern are NGC 3786, NGC 5426 and NGC 4622 (Thomasson et al. 1989; Byrd, Freeman, & Buta 2002). By χ^2 fitting the model prediction of Eq. 8 to the measured angular offsets $\Delta\phi(r)$ in all radial bins of a galaxy, we derive best-fit values for $t_{\text{HI}\rightarrow 24\mu\text{m}}$ and Ω_p .

The $\Delta\phi(r)$ data and the resulting best-fits are shown in Figure 4, with the resulting best-fit values listed in Table 2. In Figure 4 we plot for all objects the radial profile of the angular offsets $\Delta\phi(r)$. The solid line represents the best fit model proscribed by Eq. 8. The square symbols in the plot represent the fitted data points from § 4.2. Looking at the ensemble results in Figure 4, two points are noteworthy: (1) the geometric offsets are small, typically a few degrees and did need high-resolution maps to become detectable, (2) the general radial dependence follows overall the simple prescription of Eq. 8 quite well.

5.2. $t_{\text{HI}\rightarrow 24\mu\text{m}}$ and R_{cor}

Because $\Delta\phi(r)$ is consistent with (and follows) the predictions of the simple geometry and kinematics in Eq. 8, the procedure adopted here turns out to be an effective method to derive the following: (1) the time lag $t_{\text{HI}\rightarrow 24\mu\text{m}}$, which should bracket the timescale needed to compress the molecular gas, trigger star formation, and heat the dust; it therefore represents also an estimate for the lifetime of star-forming molecular clouds; (2) the kinematic pattern speed Ω_p of the galaxy spiral pattern and, equivalently, the corotation radius R_{cor} .

We now look at the ensemble properties of the resulting values for $t_{\text{HI}\rightarrow 24\mu\text{m}}$ and R_{cor} . The scatter of the individually fitted $\Delta\phi$ points is significantly larger than their error bars (as shown in Fig. 4), which may be due to the galactic dynamics being more complex than our simple assumptions. For example, the pattern speed may not be constant over the entire disk or there may be multiple corotation radii and pattern speeds, as, for instance, found by numerical simulations (Sellwood & Sparke 1988) and observed in external galaxies (Hernández et al. 2005).

⁵ <http://www.python.org>

⁶ Found at URL:

<http://zwicky.as.arizona.edu/~cyp/work/galfit/galfit.html>

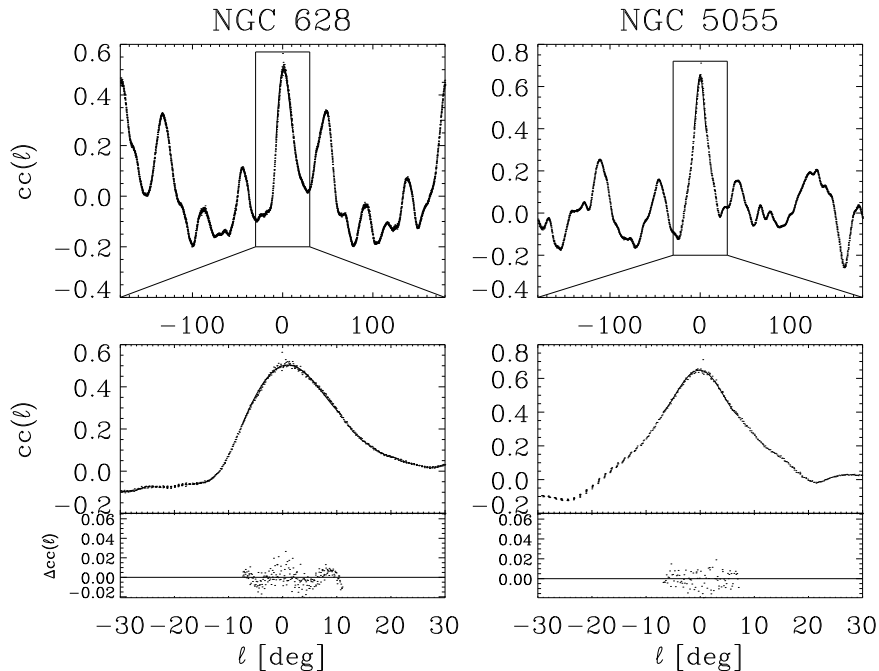


FIG. 3.— Representative examples for the determination of the azimuthal HI–24 μm offset: shown is the cross-correlation $cc(\ell)$ of the two functions $f_{\text{HI}}(\phi_k, \hat{r})$ and $f_{24\mu\text{m}}(\phi_{k-\ell}, \hat{r})$, as a function of azimuth offset ϕ at a fixed radius \hat{r} . The present example shows the $cc(\ell)$ profile calculated for NGC 628 at $\hat{r} \simeq 2'$ ($\simeq 4.2$ kpc) and NGC 5055 at $\hat{r} \simeq 2.6'$ ($\simeq 6.4$ kpc), in the left and right columns, respectively. Top panel: the $cc(\ell)$ profile in the entire range $[-180^\circ, 180^\circ]$; bottom panel: a zoom of the range $[-30^\circ, 30^\circ]$. We considered an adequate range greater than the width of the $cc(\ell)$ profile around ℓ_{max} and interpolated $cc(\ell)$ locally ($\sim \pm 10^\circ$ in the two example plots) with a fourth-degree polynomial $p_4(\ell) = \sum_{n=0}^4 a_n \ell^n$, and calculated numerically the peak value ℓ_{max} . The bottom panel shows the fit residuals overplotted around the zero level.

TABLE 2
CHARACTERISTIC TIMESCALES $t_{\text{HI} \rightarrow 24\mu\text{m}}$ AND PATTERN SPEED Ω_p RESULTING FROM A χ^2 FIT OF THE OBSERVED ANGULAR OFFSET VIA EQUATION 1

Obj. Name	Alt. Name	$t_{\text{HI} \rightarrow 24\mu\text{m}}$ [Myr]	Ω_p [km s $^{-1}$ kpc $^{-1}$]	R_{cor}/R_s	Ω_p [km s $^{-1}$ kpc $^{-1}$]
NGC 2403		1.4 ± 0.5	30 ± 4	2.8 ± 0.3	
NGC 2841		4.4 ± 0.5	42 ± 2	2.8 ± 0.1	
NGC 3031	M81	$0.5 \pm 0.3^\dagger$	$27 \pm 13^\dagger$	2.3 ± 1.4	24^a
NGC 3184		1.8 ± 0.4	38 ± 5	2.3 ± 0.5	
NGC 3351	M95	2.2 ± 0.3	38 ± 3	2.3 ± 0.4	
NGC 3521		2.9 ± 0.4	32 ± 2	3.6 ± 0.2	
NGC 3621		$2.3 \pm 1.3^\dagger$	$31 \pm 11^\dagger$	2.8 ± 1.0	
NGC 3627	M66	3.1 ± 0.4	25 ± 4	3.0 ± 0.5	
NGC 5055	M63	1.3 ± 0.3	20 ± 5	3.8 ± 1.5	$30 - 40^b$
NGC 5194	M51	3.4 ± 0.8	21 ± 4	1.5 ± 0.6	$38 \pm 7^c, 40 \pm 8^d$
NGC 628	M74	1.5 ± 0.5	26 ± 3	2.2 ± 0.4	32 ± 2^e
NGC 6946		$1.3 \pm 0.3^\dagger$	$36 \pm 4^\dagger$	1.7 ± 0.4	$39 \pm 9^c, 42 \pm 6^d$
NGC 7793		$1.2 \pm 0.5^\dagger$	$40 \pm 10^\dagger$	2.5 ± 0.9	
NGC 925		5.7 ± 1.6	11 ± 1.0	2.1 ± 0.2	7.7^f

NOTE. — The error bars are evaluated via a Monte Carlo method. The timescales $t_{\text{HI} \rightarrow 24\mu\text{m}}$ listed in this table are summarized in the histogram in Figure 5. The corotation radius to exponential scale radius R_{cor}/R_s ratios are summarized in Figure 6. We list for comparison in the last column other measurements of the pattern speed: (a) Westpfahl (1991); (b) Thornley & Mundy (1997); (c) Zimmer, Rand, & McGraw (2004); (d) Hernández et al. (2004); (e) Sakhibov & Smirnov (2004); (f) Elmegreen, Wilcots, & Pisano (1998). Addressing to the discussion on pattern speeds in § 6.2, we tag as bad fit those galaxies (indicated with the \dagger symbol) where the fit is not reliable.

Even though a considerable intrinsic scatter characterizes $\Delta\phi(r)$ for most of our sample galaxies, and the error bars of $t_{\text{HI} \rightarrow 24\mu\text{m}}$ listed in Table 2 are typically $> 15\%$, the histogram of the characteristic timescales $t_{\text{HI} \rightarrow 24\mu\text{m}}$ in Figure 5 shows overall a relatively small spread for a sample of 14 galaxies of different Hubble types: the timescales $t_{\text{HI} \rightarrow 24\mu\text{m}}$ occupy a range between 1 and 4 Myr for almost all the objects.

The solid curve in Figure 4, representing the prescrip-

tion of Eq. 8, intersects the horizontal axis at the corotation radius R_{cor} , which can be formally derived by inverting Eq. 8 at $\Delta\phi = 0$. We report in Table 2 the ratio between R_{cor} and the exponential scale length R_s for each object and show this result in Figure 6. Comparisons of our pattern speed Ω_p measurements with other methodologies (e.g. Tremaine & Weinberg 1984) are listed in Table 2. The differences with our results may arise since the Tremaine–Weinberg method assumes the continuity con-

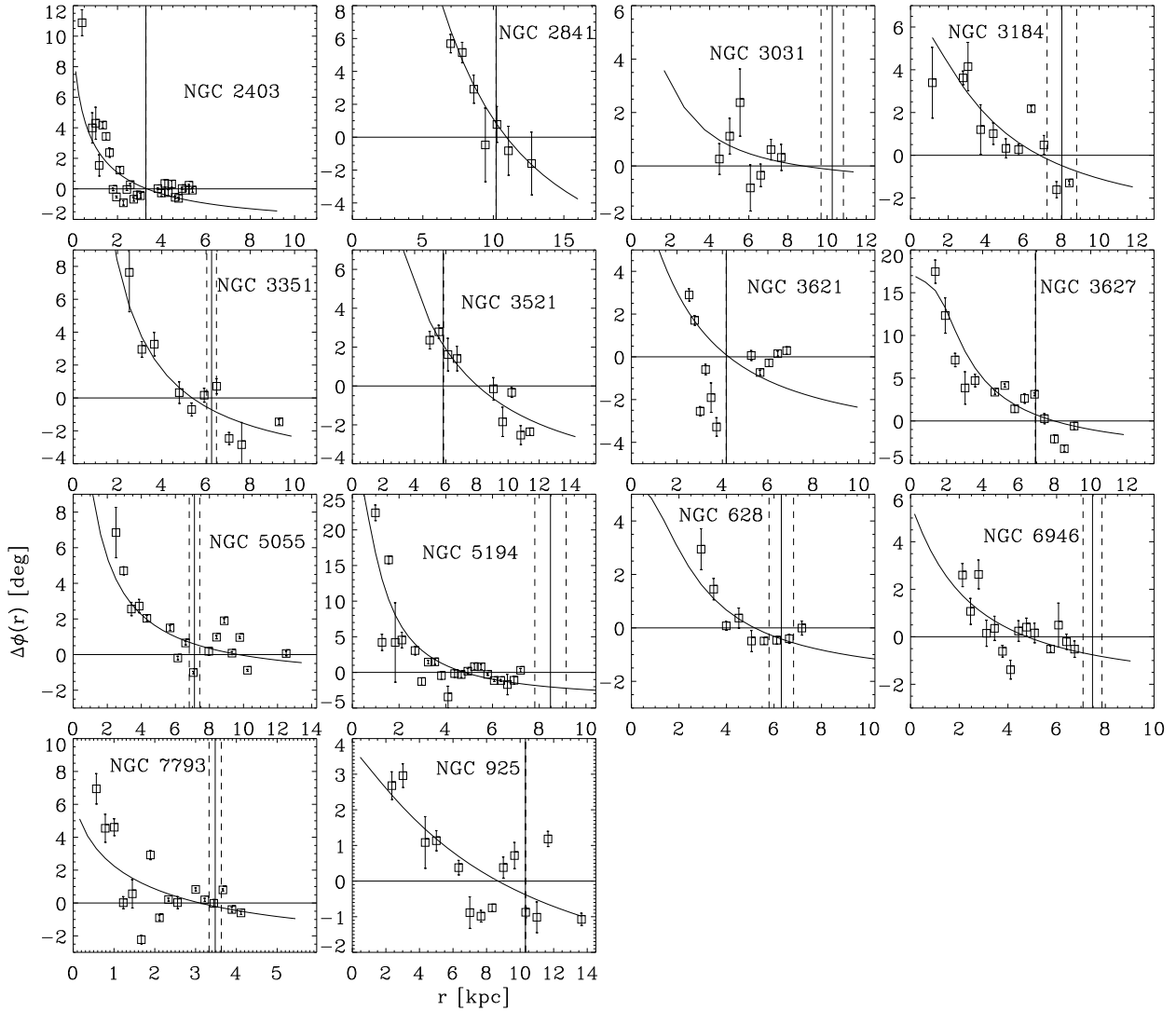


FIG. 4.— Radial profiles for the angular offset HI \rightarrow 24 μ m for the entire sample, obtained by sampling face-on HI and 24 μ m maps concentric rings and cross-correlating the azimuthal profiles for each radius. The solid line is the best-fit model to the observed data points, denoted by squared symbols, which has been obtained by χ^2 minimization of Eq. 8; the solid curve intersects the horizontal axis at corotation (defined as $\Delta\phi = 0$). The solid and dashed vertical lines indicate the $2.7 R_s \simeq R_{\text{cor}}$ value and error bars, derived by Kranz, Slyz, & Rix (2003).

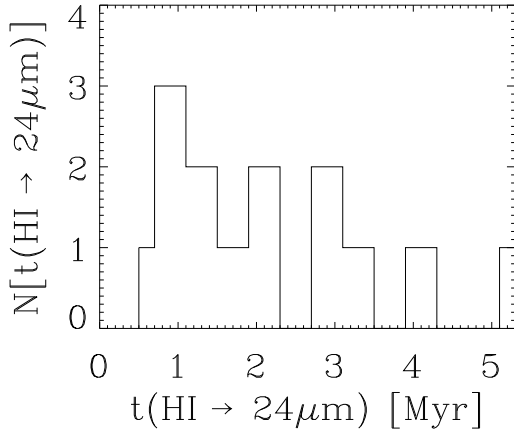


FIG. 5.— Histogram of the timescales $t_{\text{HI}\rightarrow 24\mu\text{m}}$ derived for the 14 sample galaxies listed in Table 1 from the fits in Figure 4 (also listed in Table 2). The timescales range between 1 and 4 Myr for almost all galaxies.

dition of the tracer, which may break down for the gas as it is easily shocked, it changes state, and it is converted into stars (Hernández et al. 2005; Rand & Wallin 2004), or it can be obscured by dust (Gerssen & Debattista 2007). Comparison of the observed non-axisymmetric motions with hydrodynamical models based on the actual stellar mass distribution (Kranz, Slyz, & Rix 2003) have found a characteristic value of $R_{\text{cor}}/R_s \simeq 2.7 \pm 0.4$ for a sample of spirals. We plot this range with dashed vertical lines in Figure 4, whereas the solid curve in each panel denotes the actual fit value of R_{cor}/R_s for each object. Figure 6 illustrates the interesting fact that the corotation values found in the present paper, $R_{\text{cor}}/R_s \simeq 2.7 \pm 0.2$, agree well with the completely independent estimates that Kranz, Slyz, & Rix (2003) derived by a different approach and for a different sample. Therefore, a generic value for the pattern speed of the dominant spiral feature of $R_{\text{cor}}/R_s \simeq 2.7 \pm 0.4$ seems robust.

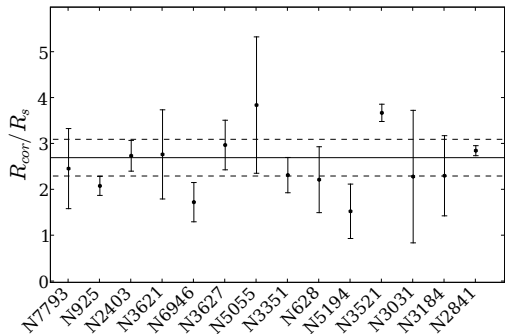


FIG. 6.— The best fit for the spiral arm corotation radius (in units of exponential scale radii) obtained by inverting the best-fit model of Eq. 1 at $\Delta\phi(r) = 0$, and evaluating R_s via a bulge-disk decomposition on either H band or $3.6 \mu\text{m}$ band images. The solid and dashed horizontal lines represent the $R_{\text{cor}}/R_s = 2.7 \pm 0.4$ value found by Kranz, Slyz, & Rix (2003). The galaxies in the plot are sorted by asymptotic rotation velocity (see Table 1), giving no indication of a correlation between dynamical mass and the R_{cor}/R_s ratio.

5.3. Comparison With CO Data

If the basic picture outlined in the introduction is correct, then the molecular gas traced by the CO, as an intermediate step in the star-formation sequence, should lie in between and have a smaller offset from the HI than the $24 \mu\text{m}$ does, but in the same direction. To check this qualitatively, we retrieve the BIMA-SONG CO maps (Helfer et al. 2003) for the galaxies NGC 628, NGC 5194, and NGC 3627. For comparison, we derive the angular offset between the CO emission and the $24 \mu\text{m}$, applying the same method described above for the HI. The results are plotted in Figure 7. The scarcity of data points (e.g., NGC 628) and their scatter, which is typically larger than the error bars, make estimates of $t_{\text{CO} \rightarrow 24 \mu\text{m}}$ and R_{cor} rather uncertain. Therefore, we simply focus on $\Delta\phi_{\text{CO} \rightarrow 24}(r)$ versus $\Delta\phi_{\text{HI} \rightarrow 24}(r)$, which is shown in Figure 7. This figure shows that the values of $\Delta\phi_{\text{CO} \rightarrow 24}$ all lie closer to zero than the values of $\Delta\phi_{\text{HI} \rightarrow 24}$.

Hence this check shows that the peak location of the molecular gas is consistent with the evolutionary sequence where the HI represents an earlier phase than the CO. In this picture the HI has a larger spatial separation with respect to the hot dust emission, except at corotation, where the three components are expected to coincide. However, it is clear that higher sensitivity CO maps are needed to improve this kind of analysis.

5.4. Analysis of Non-Circular Motions

So far we have carried out an analysis that is based on the assumption of circular motions. We quantify here non-circular motions and determine to what extent their presence affects the estimate of the timescales $t_{\text{HI} \rightarrow 24 \mu\text{m}}$, which scale with $\Delta\phi$. In the classic picture (e.g., R69), the radial velocity of the gas is reversed around the spiral shock, so that the material is at nearly the same galactocentric radius before and after the shock. Gas in galaxies with dynamically important spiral arms does not move on circular orbits, though. Shocks and streaming motions transport gas inwards, and gas orbits undergo strong variations of direction. If a continuity equation for a particular gas phase applies, it implies that in the rest frame of the spiral arm, the change of relative velocity perpendicular to the arm v_{\perp} is proportional to the arm to

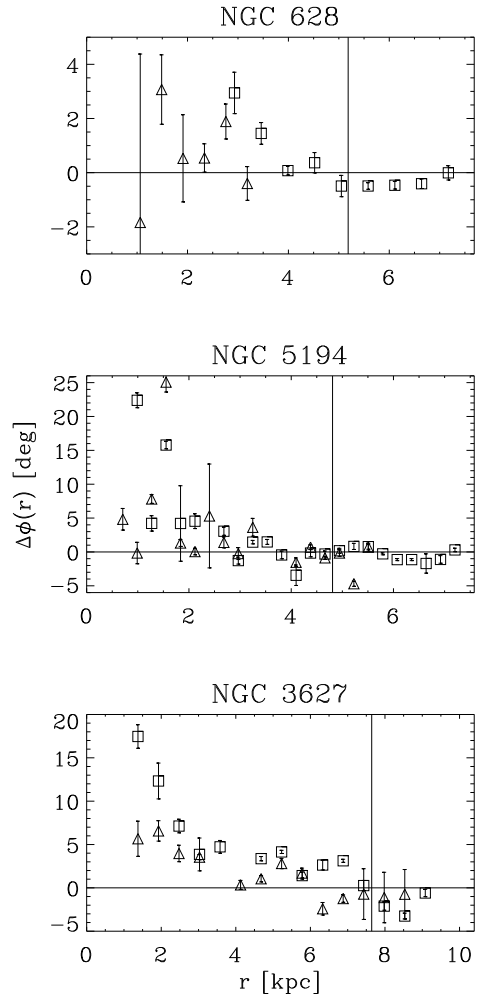


FIG. 7.— Comparison of the angular offsets obtained for $\text{HI} \rightarrow 24 \mu\text{m}$ (squares) and $\text{CO} \rightarrow 24 \mu\text{m}$ (triangles) for the galaxies NGC 628, NGC 5194, and NGC 3627. CO maps are taken from the BIMA-SONG survey. The solid vertical line in each panel indicates the position of corotation as obtained by χ^2 fitting of Eq. 1 for the HI. These results are qualitatively consistent with a temporal star-formation sequence $\text{HI} \rightarrow \text{CO} \rightarrow 24 \mu\text{m}$.

pre-arm mass flux ratio (for a recent illustration in M51 see Shetty et al. 2007, hereafter S07). For example, for an orbit passing through an arm with mass density contrast of 10, v_{\perp} would drop by the same factor, producing a net inward deflection of the orbit. We do note that the gas continuity equation may not actually be valid, since stars may form, or the gas may become molecular or ionized. Non-circular motions could modify the simplified scheme of Fig. 1. If the orbit is inward bound near the arm, the path of the material between the HI and the $24 \mu\text{m}$ arm components is larger than that previously assumed for circular orbits. We reconsider the scheme of Fig. 1 for a non-circular orbit in the frame corotating with the spiral pattern as illustrated in Fig. 8. Here, the material moves not along a line at constant radius r , but along a line proceeding from a larger radius $r + dr$, specifically from the point A (see Fig. 8) on the HI arm toward the point B on the $24 \mu\text{m}$ arm, where the two parallel horizontal lines denote the galactocentric distances $r + dr$ and r . The material departs from A with an angle α inwards (if the material were to proceed instead from an inner radius, then α is directed outwards). If α is

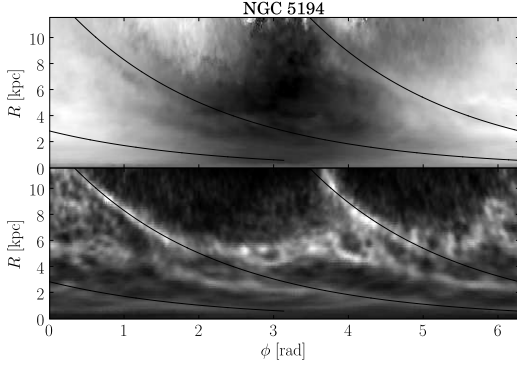


FIG. 9.— The figure illustrates logarithmic spirals of the form $\psi = \phi_{\text{arm}} - \phi_0 = \ln(R_{\text{arm}}/R_0)$ where the observed velocity v_{obs} is extracted in order to be fitted to Eq. 13 and obtain the v_R and v_ϕ velocity components (see § 5.4). The top and bottom panels represent the projection into a polar coordinates system (R, ϕ) of the observed HI line-of-sight velocity field and the HI column density map, respectively, for the galaxy NGC 5194. The solid lines represent logarithmic spiral arms with phases $\psi = \phi_{\text{arm}}$ and $\psi = \phi_{\text{arm}} \pm 180^\circ$. In the top panel, the gray scale image of the velocity field indicates velocity values from -90 km s^{-1} (dark) to $+90 \text{ km s}^{-1}$ (light). The velocity map in figure is not deprojected for inclination effects, which are instead taken into account in Eq. 13. The coordinate $\phi = 0$ represents the kinematic position angle of the galaxy.

After calculating the corrected offsets $\Delta\phi$ from Eq. 9, and fitting Eq. 8 to the values $\Delta\phi$, we find that the timescale $t_{\text{HI} \rightarrow 24 \mu\text{m}}$ and the pattern speed Ω_p do not change significantly—the differences are below the error bars for the three galaxies. Note that the data points where $v'_\phi \simeq 0$, that is where Eq. 10 diverges, are not excluded from the fit. The results of these fits are listed in Table 3 and plotted in Fig. 10. We also find that the radial displacements,

$$dr \simeq r \tan[\Delta\phi'(r)] k(r) \sin[\alpha(r)], \quad (14)$$

are typically as small compared to the radial steps of $\Delta\phi'$, i.e. $|dr| < 70 \text{ pc}$ for all r for NGC 5194. In § 4.2 we calculated $\Delta\phi'$ through Eq. 7, hence not only within the spiral arms, but also as intensity-weighted mean across all the azimuthal values. If we were to calculate the angle-averaged value $\Delta\phi'$ from the average $\langle v_R \rangle$ and $\langle v_\phi \rangle$ weighted by the product $\text{HI} \times 24 \mu\text{m}$, which is the weighting function of the cross-correlation, we find $\alpha \simeq 0$ for all radii and a correction $k(r)$ even closer to unity than over a region limited to the arms. With this approach we obtain $0.95 < k(r) < 1.05$ for NGC 5194.

After exploring the two extreme cases, (1) simple model of circular orbits and (2) streaming motions near spiral arms for galaxies with prominent spiral structure—where these effect are supposed to be the largest—we find that the implied timescales $t_{\text{HI} \rightarrow 24 \mu\text{m}}$ do not vary significantly. By estimating the streaming motions in three galaxies from our data set, we find that the correction $k(r)$ which we must apply to the angular offset measurements in the scheme of circular orbits is generally near unity. Non-circular motions do not greatly affect the offset measurements $\Delta\phi$ for the galaxies with the most prominent spiral arms of our data set, where we expect indeed the highest deviations from circular orbits, suggesting that, since $t_{\text{HI} \rightarrow 24 \mu\text{m}} \propto \Delta\phi$, the timescales $t_{\text{HI} \rightarrow 24 \mu\text{m}}$ will not vary by more than a factor of 1.5.

However, these conclusions should be viewed cautiously, since (1) we are assuming that v_R and v_ϕ can be

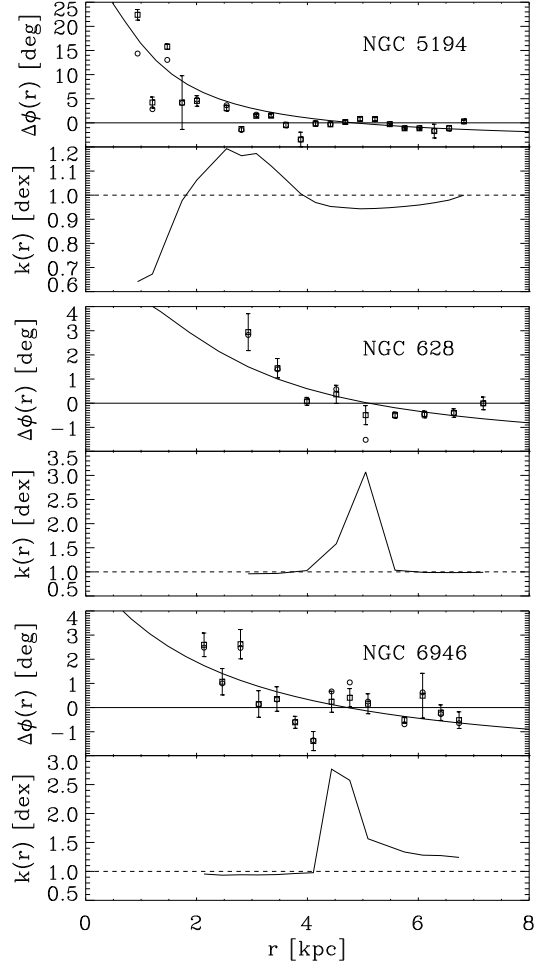


FIG. 10.— Correction factor $k(r)$ from Eq. 12, as applied to the angular offset measurement for the galaxies NGC 5194, NGC 628, and NGC 6946. Bottom panels: the solid curve represents the correction factor $k(r) = \cos \beta / \cos(\beta + \alpha)$ as a function of radius. Top panels: the squares denote the angular offset measurements $\Delta\phi'$ of Fig. 4 calculated assuming circular orbits, the circles denote $\Delta\phi$ after correction, and the solid curve represents the model fit of Eq. 8 to the corrected offset values.

obtained by fitting Eq. 13, and (2) we do not account for beam effects. While the presence of non-circular motions produces apparent radial variations of inclination and position angle, our estimates are suggesting that these effects do not influence much the determination of the timescales. Yet, tidal interactions could ensue physical variations of inclination and position angle, thus of the actual geometry of the observed velocities. Although we note that among the sample galaxies only NGC 3031 (M81), NGC 3627, NGC 5055, and NGC 5194 are affected by tidal interaction. Moreover, we do not consider extra-planar motions due to the implied numerical difficulties. For instance, to include a vertical velocity component v_z into Eq. 13 would introduce a degeneracy while fitting v_R , v_ϕ , and v_z , and a degeneracy in the geometry of the motions, rendering the estimates of the timescales uncertain. However, after subtracting a circular orbit model from the observed velocity field of the galaxy NGC 3184, an inspection of the velocity residuals reveals deviations from circular motions of $\sim 5\text{--}10 \text{ km s}^{-1}$ amplitude, and about zero near the spiral arms. Considering that NGC 3184 is nearly face-on ($i = 16^\circ$), then

TABLE 3
CHARACTERISTIC TIMESCALES $t_{\text{HI} \rightarrow 24 \mu\text{m}}$ AND PATTERN SPEED Ω_p RESULTING FROM A χ^2 FIT TO THE ANGULAR OFFSETS $\Delta\phi$ AFTER CORRECTION FOR NON-CIRCULAR MOTIONS FOLLOWING THE PRESCRIPTIONS IN SECTION 5.4

Obj. Name	Alt. Name	$t_{\text{HI} \rightarrow 24 \mu\text{m}}$ [Myr]	Ω_p [km s ⁻¹ kpc ⁻¹]
NGC 5194	M51	3.3 ± 0.6	20 ± 3
NGC 628	M74	1.4 ± 0.5	26 ± 3
NGC 6946		1.1 ± 0.3	36 ± 4

NOTE. — The best fits and the corrections are plotted in Fig. 10. In comparison with the values listed in Table 2, $t_{\text{HI} \rightarrow 24 \mu\text{m}}$ and Ω_p differ by less than their corresponding error bars.

vertical motions should not exceed 5–10 km s⁻¹. The beam deconvolution, on the other hand, would enlarge the uncertainties on separating v_R and v_ϕ , but we rely on a resolution size limit which is far below the typical thickness of a spiral arm and allows us to resolve fine sub-structures within the arms. We also rely on a large number of data points—several hundred to several thousand depending on the galactocentric radius.

6. DISCUSSION

By analyzing the angular offsets between HI and 24 μm in the context of a simple kinematic model, we found short timescales, $t_{\text{HI} \rightarrow 24 \mu\text{m}}$, as summarized in the histogram of Figure 5 and in Table 2. The implied characteristic timescales for almost all sample galaxies lie in the range 1–4 Myr. This result sets an upper limit to the timescale for massive star formation under these circumstances, since we are observing the time lag between two phases: *a*) the atomic gas phase, which subsequently is compressed into molecular clouds and forms clusters of young, embedded, massive stars, and *b*) the warm dust phase, produced by heating from young stars, whose UV radiation is reprocessed by the dust into the mid-IR, as observed at 24 μm . For the few objects where there are suitable CO data, we checked that this geometric picture also holds for the molecular phase.

6.1. Timescales Derived from Pattern Offsets

Egusa, Sofue, & Nakanishi (2004) used the same angular offset technique to compare CO and H α emission. They report timescales $t_{\text{CO} \rightarrow \text{H}\alpha} \simeq 4.8$ Myr for the galaxy NGC 4254 (not in our sample). The H α traces a later evolutionary stage than the warm dust emission, which can indicate the presence of a young cluster still enshrouded by dust. Therefore, the H α and the dust emission are expected to be separated by the time needed to remove the dusty envelope, though they are observed to be spatially well correlated (Wong & Blitz 2002; Kennicutt 1998). Prescott et al. (2007) found a strong association between 24 μm sources and optical HII regions in SINGS galaxies. Also infrared sources located on top of older, UV-bright, clusters that do not have H α emission are rare. Since Prescott et al. (2007) suggest that the break out time from dust clouds is short (~ 1 Myr), we do not expect a strong offset. Egusa, Sofue, & Nakanishi (2004) derived the angular offset by subjective assessment of the separation of the intensity peaks. They report that this may be a source of systematic errors, since they cannot detect by eye, the angular phase differences less than a certain threshold and in turn, their results would possibly be an upper limit. Given these considerations, the timescales derived in this paper are likely consistent with the conclusions of

Egusa, Sofue, & Nakanishi (2004).

Rots (1975) and Garcia-Burillo, Guelin, & Cernicharo (1993) found time lags of ~ 10 Myr for M81 and M51, respectively. In particular, Rots applied the angular offset method to the dust lanes and H α . This may be in part problematic since the dust absorption in the optical bands only traces the presence of dust and it is unrelated to the warm dust emission due to star-formation onset. Garcia-Burillo et al. measured the spatial separation projected on the sky between CO and H α and not the azimuthal offset.

Allen (2002) has argued that HI is a photodissociation product of UV shining on molecular gas, so it should be seen between the CO and UV/H α regions. Allen et al. (1986) observed HI between spiral arm dust lanes and HII regions. However, Elmegreen (2007) points out that there is no time delay between dust lanes and star formation: dust lanes may only represent a heavy visual extinction effect and may not be connected to star-formation onset. Our finding that CO is situated between HI and hot dust (i.e. Fig. 7) stands in conflict with the predictions of the model proposed by Allen (2002).

The evolutionary timescales of the ISM phases, especially for star formation, are not well constrained. The observational results of the last few decades, arrive at different and, in some cases, controversial conclusions. The discrepancies might in part be attributed to effects of limited resolution (see § 6.3). This suggests that higher resolution and sensitivity maps, especially for the CO emission, are needed to improve the presented technique in the future.

6.1.1. Photodissociation of H₂

We argue that illumination effects of UV radiation shining on molecular and dusty regions cannot photodissociate molecules in order to produce the observed peaks of HI—which correspond to typical surface densities of several solar masses per pc². First, the mean free path of the UV photons is remarkably short, typically ~ 100 pc. The presence of dust, particularly abundant in disk galaxies, is the main source of extinction in particular within spiral arms, where we observe the peak of dust emission. Second, none of the galaxies from our data set presents prominent nuclear activity, whose UV flux could ionize preferentially the inner surfaces of the molecular clouds. Also, we exclude that UV radiation from young stellar concentrations can ionize preferentially one side of the clouds causing HI and CO emissions to lie offset with respect to each other, which we instead interpret as due to an evolutionary sequence. In fact, if the light from young stars effectively produces HI by photodissociation of H₂, then the neutral to molecular gas fraction is expected to increase with star-formation rate per unit area,

Σ_{SFR} , as a consequence of the increasing UV radiation flux. Yet, the HI to H₂ ratio decreases with increasing Σ_{SFR} , as also shown, for example, in Kennicutt et al. (2007) for the galaxy M51. Moreover, the HI density does not vary much as a function of Σ_{SFR} (Kennicutt 1998).

6.2. Pattern Speeds

The results of the fits in Figure 4 are consistent with the existence of a kinematic pattern speed for the considered galaxies, and are suggesting that the spiral pattern must be metastable at least over a few Myr or, strictly speaking, quasi-stationary. If the apparent spiral structure seen in young stars were produced by stochastic self-propagating star formation (e.g. Gerola & Seiden 1978; Seiden & Gerola 1982) and shear, without an underlying coherent mass perturbation, then presumably we would not observe the systematic radial variation of the offsets, seen in Figure 4, in particular not that the offset changes sign at $R \simeq 2 - 3 R_{\text{exp}}$. Our results, however, do not exclude the stochastic star-formation mechanism to occur, rather that this is not the dominant trigger of star formation. The spiral pattern might be the manifestation of full wealth of modes of propagating density waves, which are continuously forming and dissolving gas clouds and structures, where, i.e. the azimuthal modes for a grand-design spiral are dominant at low orders (e.g., $m = 2, 3, 4$). If the spiral structure is quasi-stationary, then it can be characterized by an instantaneous pattern speed to first order—at least over a timescale much shorter than the orbital time. This is opposed to density waves dynamically driven by bars or interaction with companions, which could last a few orbital times. Note, however, that our analysis holds approximately in both possible cases.

Some of the fits in Figure 4 do not accurately mirror the trend of the observed data points, where the scatter is so large that it renders the interpretation problematic. In particular, we could designate as a bad fit the results for the galaxies NGC 3031, NGC 3621, NGC 7793, and NGC 6946 (Table 2). We also note that the pattern speed obtained in this paper for the galaxies NGC 5055 and NGC 5194 disagree with previous independent measurements (e.g. Thornley & Mundy 1997; Zimmer et al. 2004). The fit for NGC 5055 presents large error bars due to the large scatter in the azimuthal offsets (see Figure 4), which may explain the differences. For NGC 5194 the large difference between our result and the Tremaine–Weinberg method prediction could be due, as mentioned in § 5.2, to the assumption of continuity for the gas. In fact, Zimmer et al. (2004) find a pattern speed $\Omega_p^Z \simeq 38 \text{ km s}^{-1} \text{ kpc}^{-1}$ that is much faster than the pattern speed predicted by the hydrodynamical models from Kranz et al. (2003), $\Omega_p^K \simeq 12 \text{ km s}^{-1} \text{ kpc}^{-1}$, using $R_{\text{cor}} \simeq 2.7 R_s$ and $R_s \simeq 1.4'$. Moreover, the presence of large variations of the azimuthal offsets as a function of radius with respect to the smoother fitted curves of Figure 4 suggests that the pattern speed may not be constant over the entire disk. Instead, the spiral pattern could be described by more than one pattern speed, implying that the delay time is not exactly the same in all parts of an individual galaxy, and not necessarily the same in all the considered galaxies. However, the off-

sets measurements and the implied pattern speeds and timescales could be statistically pointing toward regions of high HI and 24 μm fluxes when using the weighting of Equation 7, therefore toward high Σ_{SFR} , ensuing the timescales to be comparable in all cases.

6.3. Is Star Formation Triggered by Spiral Waves?

Addressing to our results (§ 5 and Fig. 4), a further aspect emerging from our analysis concerns the same general behavior displayed by an heterogeneous sample of galaxies going from grand-design (e.g. NGC 5194) to flocculent morphologies (e.g. NGC 2841 and NGC 5055, see also Fig. 3 for an example comparison). Visual examination of the IR band images for our sample galaxies (e.g. at 3.6 μm) indicates that almost all have two-arm or multi-arm coherent spiral arms; for none of these galaxies the spiral structure is so chaotic as to be characterized as flocculent. Moreover, both types of galaxies from our sample display comparable integrated star-formation rates. Grand-design density waves are not likely to be the primary trigger of star formation, since a substantial portion of stars are also formed in the inter-arm regions (Elmegreen & Elmegreen 1986). The concentration of young stellar populations near prominent spiral arms is rather an effect of kinematics (Roberts 1969). Grand-design and flocculent galaxies exhibit the same intrinsic self-similar geometry (Elmegreen, Elmegreen, & Leitner 2003). The difference between these two types of galaxies is only dictated by a different distribution of azimuthal modes. Large scales structures (low-order modes) are the dominant features in grand design. However, the short timescales suggest that the physical scales where star formation occurs are rather small, since this time delay cannot exceed the free-fall time. Weak density waves, those described by high-order azimuthal modes, not necessarily grand-design modes, are likely to facilitate the growth of super-critical structures which end in star-forming events. In galaxies morphologically classified as flocculent and grand design, the mechanism that triggers star formation must be the same—gravitational instability. Direct compression of gas clouds is indeed able to locally trigger star formation.

The sizes of the structures of active star formation, however, are not representative of the timescales involved. Star-forming regions are organized hierarchically according to the small-scale turbulent motions of gas and stars, where the dynamical time varies as a function of the local scale sizes (Efremov & Elmegreen 1998; Ballesteros-Paredes et al. 1999). The improved accuracy of recent observational techniques, e.g. THINGS and SINGS, allows us to observe smaller and smaller structures, which evolve thus more rapidly and are characterized by shorter timescales. Stellar activity and turbulence limit the lifetime of molecular clouds by causing the destruction of the parent cloud and the cloud dispersal, respectively. This lifetime, typically 10 – 20 Myr, drops by a factor of ~ 10 for the star-forming clouds. Moreover, star formation begins at high rate in only a few Myr, appearing in large structures of O-B complexes—beads on a string—of few hundred pc scales, and remaining active for ~ 30 –50 Myr, but with a gradually decreasing star-forming rate, until the complete quenching (Elmegreen 2007). The timescales measured here refer to the very initial phase of star formation, specifically

when star-formation rate is the highest—traced by $24\ \mu\text{m}$ peak emission. The time delay $t_{\text{HI}\rightarrow 24\ \mu\text{m}}$ needs not to represent the average time difference between these two phases, especially if there is a gradually declining tail of star-formation activity, taking longer than $t_{\text{HI}\rightarrow 24\ \mu\text{m}}$. If much of the star formation were actually occurring within our short $t_{\text{HI}\rightarrow 24\ \mu\text{m}}$ estimate, then star formation would have to be inefficient to avoid conflicts with the short-term depletion of the gas reservoir.

6.4. Can We Rule Out Timescales of 10 Myr?

Since the $24\ \mu\text{m}$ emission traces the mass-weighted star-formation activity, the timescale $t_{\text{HI}\rightarrow 24\ \mu\text{m}}$ measures the time for star clusters to form from HI gas, but it does not show that all molecular clouds live only ~ 2 Myr. It might show that the bulk of massive stars that form in disks has emerged from molecular clouds that only lived ~ 2 Myr, though there could still be molecular clouds that live an order of magnitude longer. The full molecular cloud lifetimes estimated for the LMC correspond to ~ 10 Myr (Mizuno et al. 2001; Yamaguchi et al. 2001), while star clusters are formed from molecular clouds in only few Myr. Yet, more recent observations suggest much slower evolution. In particular, Blitz et al. (2007) propose molecular cloud lifetimes for the LMC as long as 20–30 Myr. In the Milky Way this timescale is estimated to be a few Myr (e.g. Hartmann, Ballesteros-Paredes, & Bergin 2001), but the examined cloud complexes, such as Taurus and Ophiuchus, have low star-formation rate and masses more than an order of magnitude lower than those studied by Blitz et al. (2007). Thus, it remains possible that our results and these previous arguments are all consistent. At high density star formation also occurs at higher rate. Blitz et al. (2007) also find that the timescales for the emergence of the first HII regions traced by $\text{H}\alpha$ in molecular clouds is $t_{\text{HII}} \sim 7$ Myr, which does not exclude that $t_{\text{HII}} \geq t_{\text{HI}\rightarrow 24\ \mu\text{m}}$, but it could be problematic with the short break out suggested by Prescott et al. (2007), since the time delay which is required between the onset of star formation (as traced by $24\ \mu\text{m}$ from obscured HII regions) and the emergence of $\text{H}\alpha$ emission would need to be large.

In conclusion, we note that the timescale $t_{\text{HI}\rightarrow 24\ \mu\text{m}}$ results from a χ^2 fit to all the data, and it is treated as a global constant individually for each galaxy, so it is not a function of radius. Globally, all the characteristic timescales $t_{\text{HI}\rightarrow 24\ \mu\text{m}}$ listed in Table 2 are ≤ 4 Myr, except one single case (NGC 925). The error bars are also relatively small: < 1 Myr for the majority of the cases. These results clearly exclude characteristic timescales $t_{\text{HI}\rightarrow 24\ \mu\text{m}}$ of the order of ~ 10 Myr, even for the highest value recorded in our data set which is NGC 925.

6.5. Theoretical Implications

The short timescale found here between the peak of HI emission and the peak of emission from young, dust-enshrouded stars has implications for two related theoretical controversies. First is the question of whether molecular clouds are short-lived, dynamically evolving objects (Ballesteros-Paredes, Hartmann, & Vázquez-Semadeni 1999, Hartmann et al. 2001; Elmegreen 2000; Ballesteros-Paredes & Hartmann 2007; Elmegreen

2007) or quasi-static objects evolving over many free-fall times (Matzner 2002; Krumholz, Matzner, & McKee 2006). The second, related question is what the rate-limiting step for star formation in galaxies is: formation of gravitationally unstable regions in the HI that can collapse into molecular clouds (Elmegreen 2002; Kravtsov 2003; Li et al. 2005, 2006; Elmegreen 2007), or formation of dense, gravitationally unstable cores within quasi-stable molecular clouds (Krumholz & McKee 2005; Krumholz, Matzner, & McKee 2006; Krumholz & Tan 2007).

The short timescales found here for the bulk of massive star formation in regions of strong gravitational instability appears to support the concept that molecular cloud evolution occurs on a dynamical time once gravitational instability has set in, and that the rate-limiting step for star formation is the assembly of HI gas into gravitationally unstable configurations. Our work does not, however, address the total lifetime of molecular gas in these regions, as we only report the separation between the peaks of the emission distributions. Molecular clouds may well undergo an initial burst of star formation that then disperses fragments of molecular gas that continues star formation at low efficiency for substantial additional time (Elmegreen 2007). Averaging over the efficient and inefficient phases of their evolution might give the overall low average values observed in galaxies (e.g. Krumholz & Tan 2007).

7. CONCLUSIONS

We have derived characteristic star-formation timescales for a set of nearby spiral galaxies, using a simple geometric approach based on the classic Roberts (1969) picture that star formation occurs just downstream from the spiral pattern, where gas clouds have been assembled into super-critical configurations. This derived timescale, $t_{\text{HI}\rightarrow 24\ \mu\text{m}}$, refers to the processes from the densest HI, to the molecular phase, to enshrouded hot stars heating the dust. The analysis is based on high-resolution 21 cm maps from THINGS, which we combined with $24\ \mu\text{m}$ maps from SINGS. We assume that the observed spiral arms have a pattern speed Ω_p . Given the rotation curve, $v_c(r) = r\Omega(r)$, this allows us to translate angular offsets at different radii between the HI flux peaks and the $24\ \mu\text{m}$ flux peaks in terms of a characteristic time difference.

At each individual point along the spiral arm we found considerable scatter between the HI and $24\ \mu\text{m}$ emission peaks. However, for each galaxy we could arrive at a global fit, using a cross-correlation technique, and derive two characteristic parameters, $t_{\text{HI}\rightarrow 24\ \mu\text{m}}$ and R_{cor} . For our 14 objects we found the general relation $R_{\text{cor}} = (2.7 \pm 0.2) R_s$, which is consistent with previous studies (e.g. Kranz, Slyz, & Rix 2003) and, more importantly, we found $t_{\text{HI}\rightarrow 24\ \mu\text{m}}$ to range between 1 and 4 Myr. Even when accounting for uncertainties, at the highest peak of star-formation rate timescales as long as $t_{\text{HI}\rightarrow 24\ \mu\text{m}} \sim 10$ Myr, which have been inferred from other approaches, do not appear consistent with our findings. At least for the case of nearby spiral galaxies, our analysis sets an upper limit to the time needed to form massive stars (responsible for heating the dust) by compressing the (atomic) gas. Therefore, it points to a rapid procession of star formation through the molecular-cloud phase

in spiral galaxies. If star formation really is as rapid as our estimate of $t_{\text{HI} \rightarrow 24 \mu\text{m}}$ suggests, it must be relatively inefficient to avoid the short-term depletion of gas reservoirs.

We thank Henrik Beuther, Mark Krumholz, Adam Leroy, and Eve Ostriker for useful discussions and suggestions. We are also grateful to the anonymous referee, whose comments helped us to improve the manuscript. The work of W.J.G.d.B. is based upon research supported by the South African Research Chairs Initiative of the Department of Science and Technology and Na-

tional Research Foundation. E.B. gratefully acknowledges financial support through an EU Marie Curie International Reintegration Grant (Contract No. MIRC-CT-6-2005-013556). M.-M.M.L. was partly supported by US National Science Foundation grant AST 03-07854, and by stipends from the Max Planck Society and the Deutscher Akademischer Austausch Dienst. This research has made use of the NASA/IPAC Extragalactic Database (NED) which is operated by the Jet Propulsion Laboratory, California Institute of Technology, under contract with the National Aeronautics and Space Administration.

REFERENCES

- Allen, R. J. 2002, in ASP Conf. Ser. 276, Seeing Through the Dust: The Detection of HI and the Exploration of the ISM in Galaxies (San Francisco, CA: ASP), 288
- Allen, R. J., Atherton, P. D., & Tilanus, R. P. J. 1986, *Nature*, 319, 296
- Ballesteros-Paredes, J., & Hartmann, L. 2007, *RevMexA&A*, 43, 123
- Ballesteros-Paredes, J., Hartmann, L., & Vázquez-Semadeni, E. 1999, *ApJ*, 527, 285
- Begeman, K. G. 1989, *A&A*, 223, 47
- Beuther, H., Churchwell, E. B., McKee, C. F., & Tan, J. C. 2007, *Protostars and Planets V (Hawaii)*, 165
- Blitz, L., Fukui, Y., Kawamura, A., Leroy, A., Mizuno, N., & Rosolowsky, E. 2007, *Protostars and Planets V (Hawaii)*, 81
- Byrd, G., Freeman, T., & Buta, R. 2002, *BAAS*, 34, 1116
- Calzetti, D., et al. 2005, *ApJ*, 633, 871
- Calzetti, D., et al. 2007, *ApJ*, 666, 870
- Cappellari, M., & Copin, Y. 2003, *MNRAS*, 342, 345
- Dale, D. A., et al. 2005, *ApJ*, 633, 857
- de Blok, W.J.G., et al. 2008, *AJ*, in press
- Dwek, E. 2005, *AIP Conf. Proc.* 761: The Spectral Energy Distributions of Gas-Rich Galaxies: Confronting Models with Data, 103
- Efremov, Y. N., & Elmegreen, B. G. 1998, *MNRAS*, 299, 588
- Egusa, F., Sofue, Y., & Nakanishi, H. 2004, *PASJ*, 56, L45
- Elmegreen, B. G. 2000, *ApJ*, 530, 277
- Elmegreen, B. G. 2002, *ApJ*, 577, 206
- Elmegreen, B. G. 2007, *ApJ*, 668, 1064
- Elmegreen, B. G., & Elmegreen, D. M. 1986, *ApJ*, 311, 554
- Elmegreen, B. G., Elmegreen, D. M., & Leitner, S. N. 2003, *ApJ*, 590, 271
- Elmegreen, B. G., Wilcots, E., & Pisano, D. J. 1998, *ApJ*, 494, L37
- García-Burillo, S., Guelin, M., & Cernicharo, J. 1993, *A&A*, 274, 123
- Gerola, H., & Seiden, P. E. 1978, *ApJ*, 223, 129
- Gerssen, J., & Debattista, V. P. 2007, *MNRAS*, 378, 189
- Glover, S. C. O., & Mac Low, M.-M. 2007, *ApJ*, 659, 1317
- Goldsmith, P. F., & Li, D. 2005, *ApJ*, 622, 938
- Goldsmith, P. F., Li, D., & Krčo, M. 2007, *ApJ*, 654, 273
- Gómez, G. C., & Cox, D. P. 2002, *ApJ*, 580, 235
- Hartmann, L. 2003, *ApJ*, 585, 398
- Hartmann, L., Ballesteros-Paredes, J., & Bergin, E. A. 2001, *ApJ*, 562, 852
- Helper, T. T., Thornley, M. D., Regan, M. W., Wong, T., Sheth, K., Vogel, S. N., Blitz, L., & Bock, D. C.-J. 2003, *ApJS*, 145, 259
- Hernández, O., Carignan, C., Amram, P., & Daigle, O. 2004, *Penetrating Bars Through Masks of Cosmic Dust*, *ASSL*, 319, 781
- Hernández, O., Wozniak, H., Carignan, C., Amram, P., Chemin, L., & Daigle, O. 2005, *ApJ*, 632, 253
- Hillenbrand, L. A., Massey, P., Strom, S. E., & Merrill, K. M. 1993, *AJ*, 106, 1906
- Hollenbach, D., & Salpeter, E. E. 1971, *ApJ*, 163, 155
- Jarrett, T. H., Chester, T., Cutri, R., Schneider, S. E., & Huchra, J. P. 2003, *AJ*, 125, 525
- Jedrzejewski, R. I. 1987, *MNRAS*, 226, 747
- Jura, M. 1975, *ApJ*, 197, 575
- Kennicutt, R. C., Jr. 1998, *ApJ*, 498, 541
- Kennicutt, R. C., Jr., et al. 2003, *PASP*, 115, 928
- Kennicutt, R. C., Jr., et al. 2007, *ApJ*, in press (arXiv:0708.0922)
- Kim, W.-T., & Ostriker, E. C. 2002, *ApJ*, 570, 132
- Kim, W.-T., & Ostriker, E. C. 2006, *ApJ*, 646, 213
- Kranz, T., Slyz, A., & Rix, H.-W. 2003, *ApJ*, 586, 143
- Kravtsov, A. V. 2003, *ApJ*, 590, L1
- Krumholz, M. R., Matzner, C. D., & McKee, C. F. 2006, *ApJ*, 653, 361
- Krumholz, M. R., & McKee, C. F. 2005, *ApJ*, 630, 250
- Krumholz, M. R., & Tan, J. C. 2007, *ApJ*, 654, 304
- Li, Y., Mac Low, M.-M., & Klessen, R. S. 2005, *ApJ*, 620, L19
- Li, Y., Mac Low, M.-M., & Klessen, R. S. 2006, *ApJ*, 639, 879
- Lin, C. C., & Shu, F. H. 1964, *ApJ*, 140, 646
- Martin, C. L., & Kennicutt, R. C., Jr. 2001, *ApJ*, 555, 301
- Matzner, C. D. 2002, *ApJ*, 566, 302
- Mizuno, N., et al. 2001, *PASJ*, 53, 971
- Mouschovias, T. C., Tassis, K., & Kunz, M. W. 2006, *ApJ*, 646, 1043
- Palla, F., & Stahler, S. W. 1999, *ApJ*, 525, 772
- Palla, F., & Stahler, S. W. 2000, *ApJ*, 540, 255
- Peng, C. Y., Ho, L. C., Impey, C. D., & Rix, H.-W. 2002, *AJ*, 124, 266
- Prescott, M. K. M., et al. 2007, *ApJ*, 668, 182
- Rafikov, R. R. 2001, *MNRAS*, 323, 445
- Rand, R. J., & Kulkarni, S. R. 1990, *ApJ*, 349, L43
- Rand, R. J., & Wallin, J. F. 2004, *ApJ*, 614, 142
- Rix, H.-W., Guhathakurta, P., Colless, M., & Ing, K. 1997, *MNRAS*, 285, 779
- Rix, H.-W., & Zaritsky, D. 1995, *ApJ*, 447, 82
- Roberts, W. W. 1969, *ApJ*, 158, 123
- Rots, A. H. 1975, *A&A*, 45, 43
- Sakhibov, F. K., & Smirnov, M. A. 2004, *Astron. Rep.*, 48, 995
- Scoville, N. Z., Polletta, M., Ewald, S., Stolovy, S. R., Thompson, R., & Rieke, M. 2001, *AJ*, 122, 3017
- Seiden, P. E., & Gerola, H. 1982, *Fundamentals of Cosmic Physics*, vol. 7, no. 3, p. 241
- Sellwood, J. A., & Sparke, L. S. 1988, *MNRAS*, 231, 25P
- Shetty, R., Vogel, S. N., Ostriker, E. C., & Teuben, P. J. 2007, *ApJ*, 665, 1138
- Smith, J. D. T., et al. 2007, *ApJ*, 656, 770
- Tan, J. C., Krumholz, M. R., & McKee, C. F. 2006, *ApJ*, 641, L121
- Tassis, K., & Mouschovias, T. C. 2004, *ApJ*, 616, 283
- Thomasson, M., Donner, K. J., Sundelius, B., Byrd, G. G., Huang, T. Y., & Valtonen, M. J. 1989, *Ap&SS*, 156, 205
- Thornley, M. D., & Mundy, L. G. 1997, *ApJ*, 484, 202
- Thronson, H. A., Jr., & Telesco, C. M. 1986, *ApJ*, 311, 98
- Toomre, A. 1964, *ApJ*, 139, 1217
- Trachternach, C., et al. 2008, *AJ*, submitted
- Tremaine, S., & Weinberg, M. D. 1984, *ApJ*, 282, L5
- Vázquez-Semadeni, E., Kim, J., Shadmehri, M., & Ballesteros-Paredes, J. 2005, *ApJ*, 618, 344
- Vogel, S. N., Kulkarni, S. R., & Scoville, N. Z. 1988, *Nature*, 334, 402
- Walter, F., et al. 2008, *AJ*, submitted
- Westpfahl, D. 1991, in ASP Conf. Ser. 18, The Interpretation of Modern Synthesis Observations of Spiral Galaxies, 175
- Williams, D. A. 2005, *JPhCS*, 6, 1
- Wong, T., & Blitz, L. 2002, *ApJ*, 569, 157
- Yamaguchi, R., et al. 2001, *PASJ*, 53, 985
- Zimmer, P., Rand, R. J., & McGraw, J. T. 2004, *ApJ*, 607, 285